vol. **34**, pp. 313–338, 1996.

Rohan, E., Mathematical modelling of soft tissues, Habilitation thesis, Pilsen 2002.

Rohan, E., Sensitivity strategies in modelling heterogeneous media undergoing finite deformation, *Math. Comput. Simul.*, vol. **61**, pp. 261–270, 2003.

Rohan, E., Modelling large deformation induced microflow in soft biological tissues, *Theor. Comput. Fluid Dyn.*, vol. **20**, pp. 251–276, 2006.

Rohan, E., Cimrman, R., and Lukeš, V., Numerical modelling and homogenized constitutive law of large deforming fluid saturated heterogeneous solids, *Int. J. Comput. Struct.*, vol. **84**, pp. 1095–1114, 2006.

Rohan, E., et al., Homogenization of biot medium with dual porosity: Multiscale bone poroelasticity, (submitted), 2009.

Showalter, R. E. and Visarraga, D. B., Double-diffusion models from a highly heterogeneous medium, *J. Math. Anal. Appl.*, vol. **295**, pp. 191–210, 2004.

Vankan, W. J., Huyghe, J. M. R. J., Slaaf, D. W., van Donkelaar, . C., Drost, M., Janssen, J. D., and Huson, A., Finite element simulation of blood perfusion in muscle tissue during compression and sustained contraction, *Am. J. Physiol.*, vol. **273**(3), pp. H1587–H1591, 1997.

International Journal for Multiscale Computational Engineering 8(1), 103–112 (2010)

UPSCALING OF PERMEABILITY OF POROUS MATERIALS: FIRST INSIGHT INTO THE EFFECT OF PORE-SPACE CHARACTERISTICS

***Xian Liu,*[1,2] *Matthias Zeiml,*[1] *Roman Lackner,*[3*] *& Herbert A. Mang*[1]**

[1]*Institute for Mechanics of Materials and Structures, Vienna University of Technology, Vienna, Austria*

[2]*Department of Geotechnical Engineering, Tongji University, Shanghai, China*

[3]*Material Technology Innsbruck, University of Innsbruck, Innsbruck, Austria*

*Address all corespondence to R. Lackner E-mail: Roman.Lackner@uibk.ac.at

The material phase "air" (pore space) in porous materials determines the amount of fluid flow into and through the material and, hence, the time scale of physical/chemical degradation processes in durability aspects of materials and structures. Hereby, the pore-space characteristics, such as pore-size distribution and pore arrangement, both being accessible via respective experimental techniques, influence the transport properties of the material. In this paper, this influence is investigated within the multiscale framework, employing a so-called random pore-network model. Hereby, random arrangements of prescribed pore-size distributions are modeled, giving – under the assumption of steady-state flow conditions – access to the macroscopic permeability of the material. More specifically, three idealized pore-size distributions, i.e., (i) two different radii and (ii) constant and (iii) normal pore-size distribution, are investigated by means of several sets of network configurations. From the obtained results, both mean value and standard deviation of the macroscopic permeability corresponding to a certain pore-size distribution are determined, giving new insight into the impact of pore-space characteristics on the permeability and its variation in porous materials.

KEY WORDS: *pore-size distribution, permeability, network model, upscaling*

1. INTRODUCTION

It is well known that the pressure-driven transport of fluids in porous materials is governed by the permeability of these materials. For example, in the case of high-temperature loading of concrete structures, vaporization of physically and chemically-bound water results in an increase of pore pressure, which in case of low transport ability causes spalling of near-surface concrete layers. This pressure-driven transport of water vapor is commonly described by Darcy's law with the permeability as the governing parameter (Zeiml, 2008).

In general, the permeability of porous materials is defined at the so-called macroscale, i.e., the scale where the material is treated as a continuum, and is related – if at all – to pore-space properties (e.g., porosity) by means of empirical relations (Mehta and Manmohan, 1980; Marchand and Gerard, 1997). More advanced models of relating macroscopic permeability properties to the material microstructure are based on digital images (Garboczi and Bentz, 1996; Sandouki and van Mier, 1997; Ye et al., 2006) and pore networks (Galle and Daian, 2000; Carmeliet et al, 1999). The accuracy of these models, however, strongly depends on the available information about the microstructure, accessible via proper experimental techniques such as mercury-intrusion porosimetry (MIP) and image analysis. These techniques give access to the pore-size distribution and the total pore vol-

1091-028X/10/$35.00

ume, which may, however, build up different pore arrangements with different permeability properties.

In this paper, the impact of the pore-size distribution and pore arrangement on the macroscopic permeability of porous materials is investigated. Taking the random nature of the pore arrangement into account, a random pore-network model is developed in order to relate the macroscopic permeability to characteristics of the pore space. The macroscopic permeability is regarded as a stochastic material property, determined from transport properties obtained from random pore networks.

The paper is organized as follows: In Section 2, the framework of the random network model, including basic model assumptions, pore-space generation, and the solution procedure of the random network, is presented. Based on results obtained from the random network model, the impact of the pore-size distribution and the pore arrangement on the macroscopic permeability is investigated in Section 3, taking three types of pore-size distributions into account.

2. MODEL DESCRIPTION

In order to build up the pore space of a porous material, the following assumptions are taken into account:

1. Each single pore of the network is treated as a tube with circular cross section. In the case of steady-state flow, the Hagen-Poiseuille law (Wikipedia; Sutera and Skalak, 1993) is used to describe fluid flow in this pore tube.
2. All pores in the network have the same length.
3. Finally, for the design of the pore network, a 2D arrangement – already capturing most features of a 3D pore structure (Carmeliet et al, 1999) – is considered in order to study the main effects of the pore-space characteristics on the macroscopic permeability. The methods developed herein, however, can also be applied to 3D network models.

Following the above assumptions, the fluid flux Q (in cubic meters per second) through a single pore of length l (in meters) and radius r (in meters) is given by the Hagen-Poiseuille law as (Wikipedia; Sutera and Skalak, 1993)

$$Q = -\frac{\pi r^4}{8\,\mu}\frac{\Delta p}{l}, \tag{1}$$

where Δp (in Pascal) is the pressure difference within the pore and μ (in Pascal times second) is the viscosity of the fluid. Based on the fluid flow in a single pore, a 2D network is used to model the pore space. Hereby, a 2D cross-squared network composed of cylindrical pores is constructed using a regular lattice (see Fig. 1, illustrating an $N \times N$ pore network, with $N = 5$).

Based on the underlying pore-size distribution, pores with different radii are placed in the network in a random manner. In the case of a continuous pore-size distribution, the finite number of available pores within the network, n_p, represents the pore-size distribution in a discretized manner. Figure 2 illustrates this approximation for a constant pore-size distribution and the respective linear cumulative pore volume represented by a finite number of pores within the network model.

For a given pore network, the macroscopic permeability can be calculated by imposing a unit pressure gradient at two opposite sides (top and bottom side, see Fig. 1) of the employed 2D network. For determination of the flux through the network, the pressures in the connection points of the single pipes (nodes) are used as state variables. Thus, the flux through the ith pore of the network system is given by the Hagen-Poiseuille law (1) as

$$q_i = -\frac{\pi r_i^4}{8\mu}\frac{\Delta p_i}{l_i}, \tag{2}$$

where Δp_i (in Pascal) is the pressure difference between the end and beginning node of the considered pore, respectively. At each node, mass conservation must hold, yielding

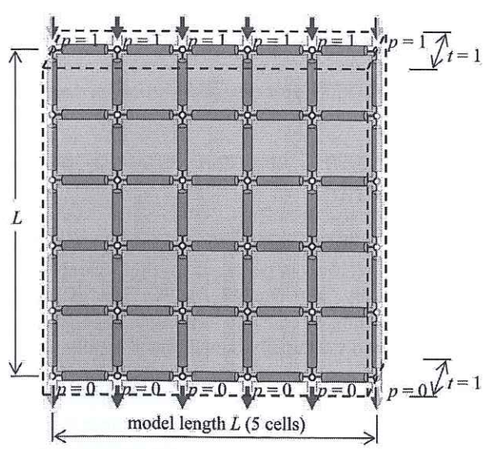

FIG. 1: Two-dimensional idealized $N \times N$ pore network for $N = 5$, consisting of $n_p = 2N(N+1)$ pores (L: size of the 2D network model)

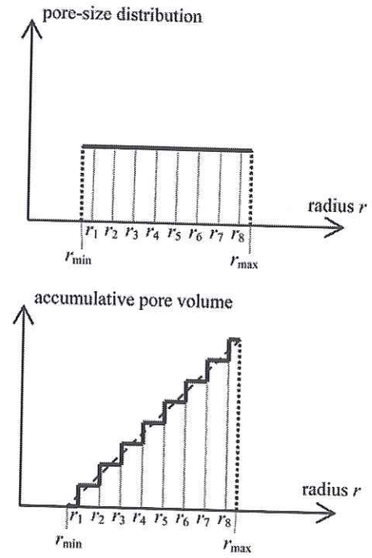

FIG. 2: Approximation of given linear accumulative pore volume (constant pore-size distribution) by eight pores

$$\sum_{i \in J_{\text{conn}}} q_i = 0, \tag{3}$$

where J_{conn} represents the set of pores connected to the considered node.

As boundary conditions, the left and right side of the network model are considered as sealed (no-flow condition), giving equal flux for the top and bottom sides of the model. Considering the initial condition of an imposed unit pressure gradient, inserting Eq. (2) into Eq. (3) gives one equation per node for determination of the unknown pressure at each node of the network model. Based on the computed pressures and, thus, fluxes through the individual pores, the overall flux through the network model, Q (in cubic meters per second), is computed as

$$Q = \sum_{i \in J_{\text{bottom}}} q_i, \tag{4}$$

where J_{bottom} represents the pores connected to the bottom side of the network model (see Fig. 1).

Finally, the effective (macroscopic) permeability K (in meters squared) of the network model is determined by Darcy's law, setting the out-of-plane dimension of the model t (in meters) to 1 m, giving

$$Q = \frac{KA}{\mu}\frac{\Delta P}{L} = \frac{K(t \times L)}{\mu}\frac{\Delta P}{L} = \frac{K}{\mu} \rightarrow K = Q\mu, \tag{5}$$

where $t = 1$ m and $\Delta P = 1$ Pa were considered, with $A = t \times L$ (in meters squared) as the cross-sectional area of the top and bottom sides, and $\Delta P/L = 1/L$ (in Pascal per meter) as the imposed unit pressure gradient. Accounting for the random arrangement of pores, the described procedure is carried out for various pore-space configurations. Let n_a be the number of considered pore arrangements; then the mean value and standard deviation can be computed for the n_a – in general differing – macroscopic permeabilities as follows:

$$\overline{K} = \frac{1}{n_a}\sum_{i=1}^{n_a} K_i \tag{6}$$

and

$$D = \sqrt{\frac{\sum_{i=1}^{n_a}(K_i - \overline{K})^2}{n_a}}, \tag{7}$$

where K_i refers to the permeability of the ith pore arrangement.

3. APPLICATION

In order to investigate the influence of the pore-size distribution on the macroscopic permeability, the following three different pore-size distributions are considered (see Fig. 3):

(a) Two-radii pore-size distribution,

$$f_V(r) = \begin{cases} f_1, r = r_1 \\ f_2, r = r_2 \end{cases} \quad \text{with} \quad f_1 + f_2 = 1 \quad \text{and} \quad r_1 \le r_2, \tag{8}$$

where f_i is the volume fraction when radius r takes the value of r_i $(i = 1, 2)$.

(b) Constant pore-size distribution,

$$f_V(r) = \frac{1}{r_{\max} - r_{\min}} \quad \text{with} \quad r_{\min} \le r \le r_{\max} \quad \text{and} \quad \overline{r} = \frac{r_{\min} + r_{\max}}{2}, \tag{9}$$

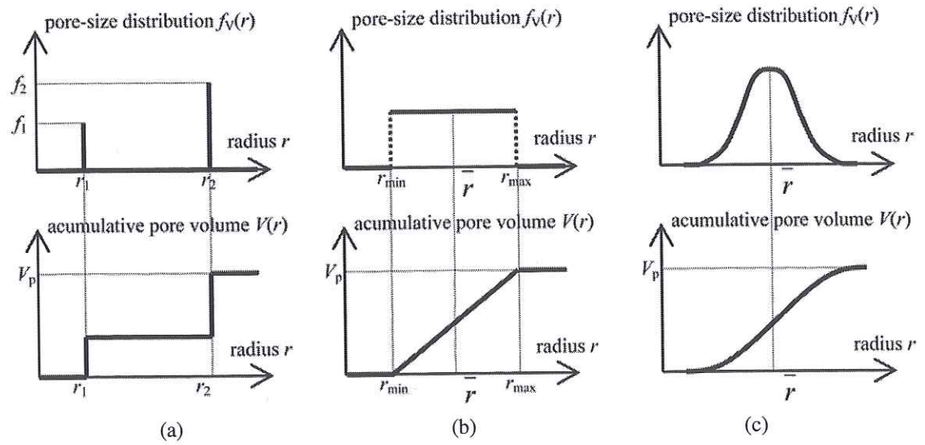

FIG. 3: Investigated pore-space configurations: pore-size distribution and accumulative pore volume for **(a)** two-radii, **(b)** constant and **(c)** normal pore-size distribution

where $\overline{r}$ is the mean radius of the pore-size distribution.

(c) Normal pore-size distribution,

$$f_V(r) = \frac{1}{\sqrt{2\pi} D_r} e^{-[(r-\overline{r})^2/(2D_r^2)]}, \quad (10)$$

with $\overline{r}$ and D_r as mean radius and standard deviation of the pore-size distribution, respectively.

Within the numerical studies, the length of each pipe was set to 50 m, giving a model length for, e.g., a network model with $N = 20$, of $L = 1000$ m. In order to focus exclusively on the effect of pore-space characteristics given by the pore-size distribution and the pore arrangement, the overall pore volume V_p (in cubic meters) is directly related to the number of pores n_p [i.e., the model size N, with $n_p = 2N(N+1)$]. This yields, e.g., $V_p = 1{,}495{,}000$ m^3 for $N = 20$ (giving $n_p = 840$ and $L = 1000$ m).

3.1 Two-Radii Pore-Size Distribution

Within the analysis of the two-radii distribution (see Fig. 3(a)), the input parameters of the model (r_1, r_2, f_1, f_2) are varied. By setting $V_p = 1{,}495{,}000$ m^3 constant, two of the four parameters can be chosen. Throughout the analyses, r_1 and f_1 were chosen as input parameters, yielding the remaining parameters as

$$f_2 = 1 - f_1 \quad (11)$$

and

$$r_2 = \sqrt{\frac{V_p(1-f_1)}{[n_p - (f_1 V_p/(r_1^2 \pi\, l))]\, \pi\, l}}, \quad (12)$$

with $n_p = 2N(N+1)$ as the number of pores and $l = 50$ m as the pore length. Starting with the case of a uniform pore-size distribution (i.e., $r_1 = r_2 = r$), the resulting pore radius is given as $r = \sqrt{V_p/(n_p \pi\, l)} = \sqrt{1{,}495{,}000/(840 \cdot \pi \cdot 50)} = 3.36$ m. Figure 4 shows radius r_2 as a function of the input parameters r_1 and f_1. For the general case of two different radii r_1 and r_2, $[n_p - (f_1 V_p/r_1^2 \pi\, l)] > 0$ in Eq. (12) yields a condition for the choice of input parameters as (see Fig. 4)

$$r_1 > \sqrt{\frac{f_1 V_p}{n_p \pi\, l}}. \quad (13)$$

In order to study the convergence behavior of the employed analysis scheme for determination of the macroscopic permeability, both network size N and the number of analyzed pore arrangements n_a are varied (see Fig. 5). For small N, the convergence behavior is not satisfactory since boundary effects (no-flow condition at left and right boundary of the network) apparently influence the results. For larger networks, the convergence behavior is

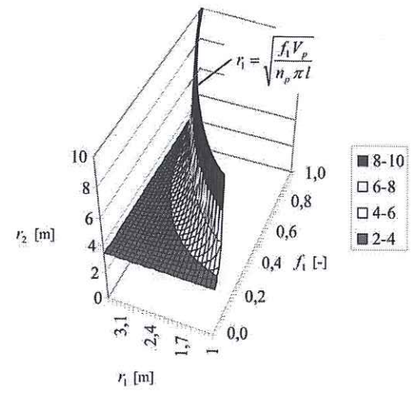

FIG. 4: r_2 as a function of input parameters r_1 and f_1 for the two-radii pore-size distribution

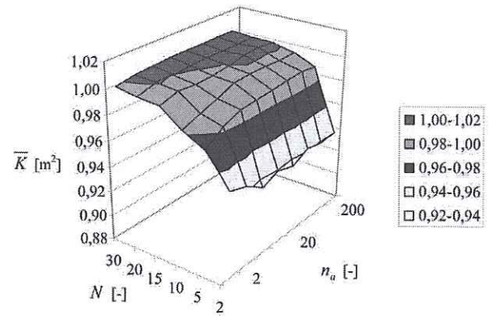

FIG. 5: Investigation of the convergence behavior of the employed analysis scheme: mean value for the permeability, $\overline{K}$, as a function of network size N and number of analyzed pore arrangements n_a (input parameters: $r_1 = 3$ m, $f_1 = 0.1$; $r_2 = 3.42$ m, $f_2 = 0.9$ according to Eqs. (11) and (12))

improved, even allowing the use of fewer pore arrangements n_a. For the subsequent analyses, $N = 20$ and $n_a = 200$ are chosen.

Based on these satisfactory observations regarding the convergence behavior of the employed analysis scheme, parameter studies are performed. Figure 6 shows representative random pore arrangements with different results for the macroscopic permeability K. The respective results for the mean value of the macroscopic permeability, $\overline{K}$, are shown in Fig. 7(a). Hereby, pore-size distributions with either $f_1 = 0$ or $r_1 = 3.36$ m refer to the special case of a uniform pore system (with $r = 3.36$ m), giving the analytically-obtained value for the permeability according to Eqs. (2) and (5) as

$$K = Q\mu = N\, q\, \mu = N \frac{\pi \cdot r^4}{8 \cdot \mu} \frac{\Delta p_i}{l_i} \mu = 20 \cdot \frac{\pi \cdot 3.36^4}{8} \frac{1}{1000} = 1.0 \text{ m}^2, \quad (14)$$

with $\Delta p_i / l_i = \Delta p / L = 1/L$. For other r_1, f_1 combinations (i.e., nonuniform pore systems), the obtained macroscopic permeability is apparently smaller, with a steep decrease of $\overline{K}$, illustrating the effect of small-size pores on the macroscopic permeability. For a given value of f_1, a decrease of r_1 results in more pores with this respective radius and therefore an increased number of so-called bottle necks within the pore system. For a given r_1, an increase in f_1 has the same effect, also reducing the macroscopic permeability. The region with $\overline{K} = 0$ refers to the above-mentioned case where condition (13) is not satisfied, i.e., no pore system can be generated. When investigating the standard deviation for the macroscopic permeability (Fig. 7(b)), a peak can be observed for certain r_1, f_1 combinations. These combinations are in the region where the diversity of the pore system is the highest. (As mentioned before, $f_1 = 0$ and $r_1 = 3.36$ m refer to the special case of a uniform pore system, leading to $D = 0$. r_1, f_1 combinations close to the region where condition (13) is not satisfied, i.e., $D = 0$ in Fig. 7(b), also lead to almost uniform pore systems.) When scaling the standard deviation by the respective mean value for the macroscopic permeability, again a peak for certain r_1, f_1 combinations is observed (see Fig. 7(c)).

3.2 Constant Pore-Size Distribution

Based on the above observations, the constant pore-size distribution (see Fig. 3(b)) is investigated in the following. Hereby, the slope of the so-obtained linear cumulative pore volume is varied (see Fig. 8), yielding (considering $V_p = 1{,}495{,}000$ m^3 = constant for $N = 20$) different r_{min},r_{max} pairs and, hence, different mean radii $\overline{r}$. For the special case of infinite slope, a uniform pore system with $r_{min} = r_{max} = \overline{r} = r = 3.36$ m is obtained.

Figure 9 shows representative random pore arrangements considered within the analyses. Figure 10 contains the analysis results with the respective permeability distributions displayed in Fig. 10(a). For decreasing mean pore radius $\overline{r} = (r_{min} + r_{max})/2$ (i.e., for increasing slope), the

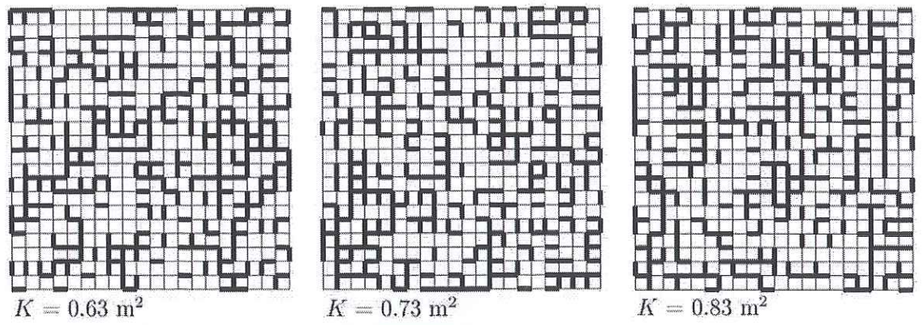

FIG. 6: Representative random pore arrangements for two-radii pore-size distribution with different results for the macroscopic permeability K (input parameters: $r_1 = 1.75$ m, $f_1 = 0.1$, $r_2 = 4.02$ m, $f_2 = 0.9$)

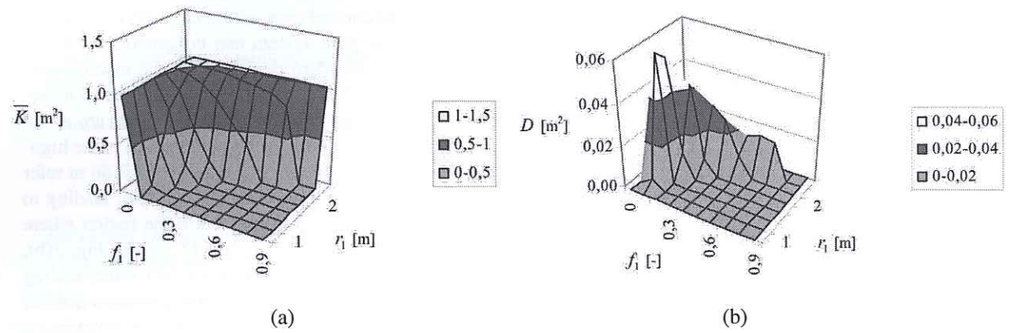

FIG. 7: Investigation of pore networks characterized by a two-radii pore-size distribution: **(a)** mean value $\overline{K}$, **(b)** standard deviation D, and **(c)** $D/\overline{K}$ as a function of r_1 and f_1

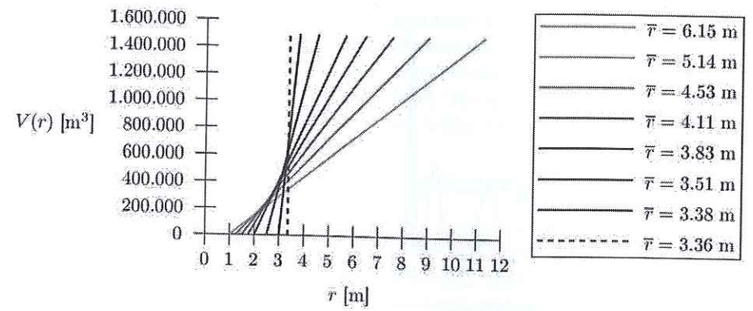

FIG. 8: Investigated constant pore-size distributions with different mean radii $\overline{r}$ (and, hence, different $r_{\min}$, $r_{\max}$ pairs), leading to a linear cumulative pore volume

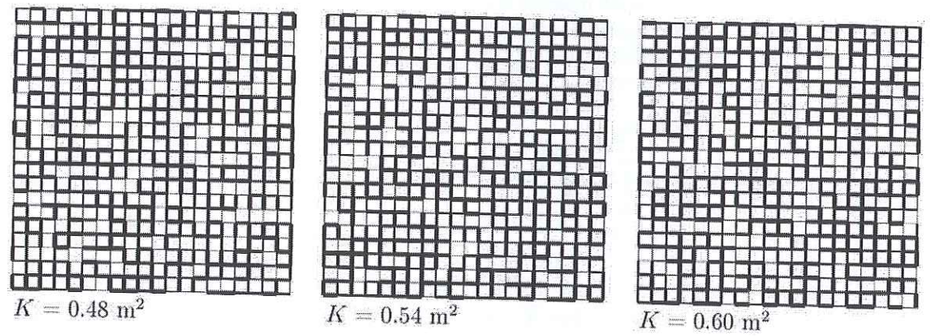

FIG. 9: Representative random pore arrangements for constant pore-size distribution with different results for the macroscopic permeability K (input parameter: mean radius $\overline{r} = 4.11$ m)

mean value for the permeability, $\overline{K}$, increases (also refer to Fig. 10(b)). This can be explained by the increasing regularity of the pore system for decreasing values of $\overline{r}$, with $\overline{K}$ approaching the respective value for a uniform pore-size distribution ($K = 1.0$ m^2, see dashed line in Fig. 10(a) as well as circle in Fig. 10(b)). In the case of increasing $\overline{r}$ and, hence, decreasing slope of the cumulative pore volume, $r_{\max}$ increases. However, only a small number of larger pores ($\overline{r} < r < r_{\max}$) are present in the network, whereas – at the same time – $r_{\min}$ decreases and hence the number of small-size pores ($r_{\min} < r < \overline{r}$) increases rapidly, reducing the macroscopic permeability. As shown in Fig. 10(a), the width of the permeability distribution (i.e., the standard deviation D) seems to have a maximum for a specific value of $\overline{r}$ (i.e., a specific slope of the cumulative pore volume). However, scaling the standard deviation by the respective mean value of the macroscopic permeability ($D/\overline{K}$, see Fig. 10(b)) shows that the deviation increases monotonously with increasing irregularity of the pore system (i.e., with increasing $\overline{r}$ or decreasing slope). Moreover, $D/\overline{K}$ approaches zero for the case of a uniform pore-size distribution (at $\overline{r} = r = 3.36$ m), since $D \to 0$ (see circle in Fig. 10(b)).

3.3 Normal Pore-Size Distribution

Within further analyses, normal pore-size distributions (see Fig. 3(c)) are investigated considering different combinations of mean pore radius $\overline{r}$ (in meters) and standard deviation D_r (in meters) (see Fig. 11), taking into account the condition of constant cumulative pore volume for a given network size, with $V_p = 1{,}495{,}000$ m^3 for $N = 20$.

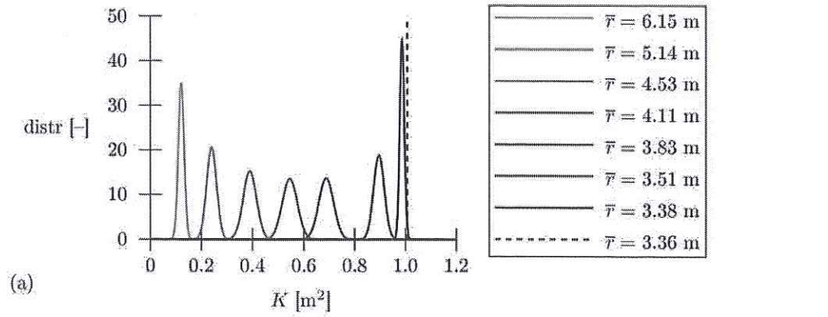

(a)

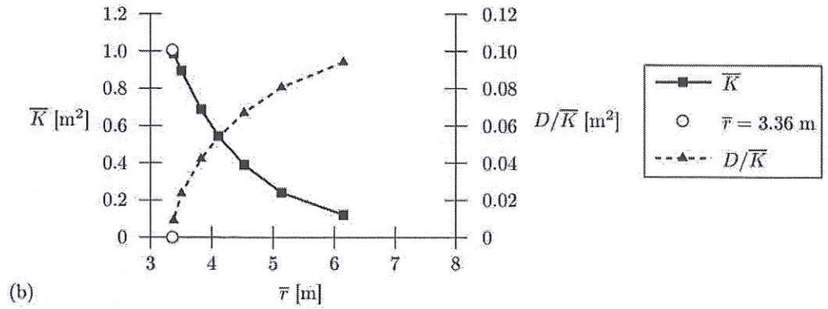

(b)

FIG. 10: Investigation of pore networks characterized by a constant pore-size distribution: **(a)** obtained permeability distributions; **(b)** mean value for the permeability, $\overline{K}$, and standard deviation D scaled by $\overline{K}$ as a function of mean pore radius $\overline{r}$

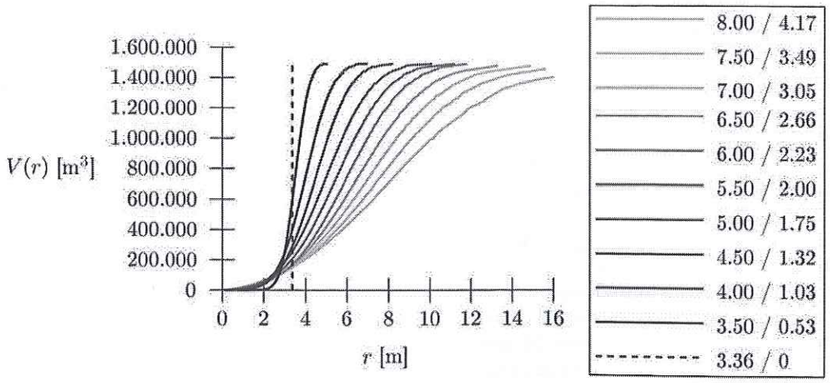

FIG. 11: Investigated normal pore-size distributions with different $\overline{r}$ and D_r (notation: $\overline{r}/D_r$)

Figure 12 shows the obtained numerical results. As observed before for the constant pore-size distribution, the mean value of the macroscopic permeability, $\overline{K}$, increases with increasing regularity of the pore system (i.e., with decreasing mean value for the radius of the normal pore-size distribution, see Figs. 12(a) and 12(b)). Additionally, the results approach the case of a uniform pore system, characterized by $\overline{r} = r = 3.36$ m and $K = 1.0$ m^2 (see Fig. 12(b)). The variation of the macroscopic permeability again seems to have a maximum for a certain normal pore-size distribution (for the performed analyses, the maximum in D refers to a mean pore radius of $\overline{r} = 4.5$ m, see Fig. 12(a)); however, when scaling the deviation of the permeability results (giving $D/\overline{K}$, see Fig. 12(b)), a monotonously increasing trend is observed up to a mean pore radius of $\overline{r} = 6$ m. For higher mean pore radii, this trend is reversed and $D/\overline{K}$ decreases again. This observation is explained by the rather small magnitude of both D and $\overline{K}$, on the one hand, and an increasing discretization error (with the cumulative pore volume – given by the discrete number of pores – starting to significantly deviate from the target value of $V_p = 1{,}495{,}000$ m^3), on the other hand. The latter also explains the observed oscillations in the scaled standard deviation shown in Fig. 12(b).

4. SUMMARY AND OUTLOOK

The transport properties of porous materials are a key parameter concerning durability aspects of materials and structures. Hence, prediction of the permeability based on information about the pore space, where the latter can be influenced during the construction process, is of high importance. In this work, a so-called random pore-network model is developed in order to determine the mean value and standard deviation for the macroscopic permeability of porous materials for different pore-size distributions. In this way, in addition to the influence of the shape of the pore-size distribution, the influence of the arrangement of

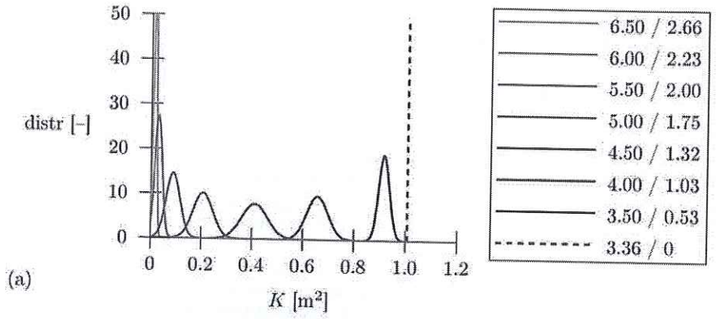

(a)

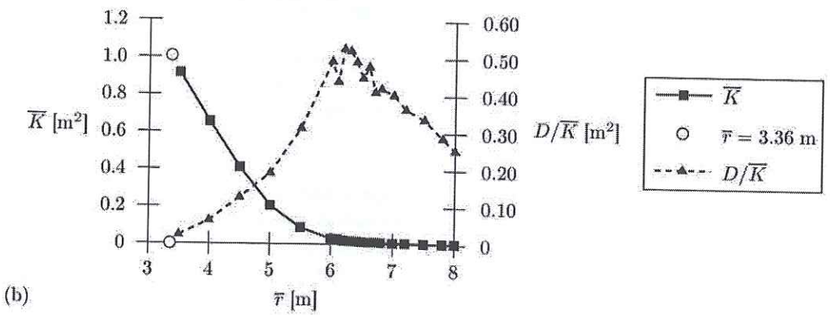

(b)

FIG. 12: Investigation of pore networks characterized by a normal pore-size distribution: **(a)** obtained permeability distributions (notation: $\overline{r}/D_r$); **(b)** mean value for the permeability, $\overline{K}$, and standard deviation D scaled by $\overline{K}$ as a function of mean pore radius $\overline{r}$

the respective pores on the macroscopic permeability is investigated.

In a first step, the developed model was applied to three idealized pore-size distributions, namely, *(i)* two-radii, *(ii)* constant and *(iii)* normal pore-size distribution. Investigation of the two-radii pore-size distribution showed that the size and volume fraction of small-size pores are the governing factors with respect to the macroscopic permeability of the pore system. Moreover, the diversity of the pore system had an effect on the stochastic nature of the permeability (i.e., the respective standard deviation). In the case of the constant pore-size distribution, the mean value for the macroscopic permeability decreased with decreasing slope of the cumulative pore volume, whereas the standard deviation of the permeability increased with respect to the mean value for the permeability at the same time. This was explained by the increasing irregularity of the pore system. Even though large-size pores become larger for decreasing slope, only a small number of these pores exist in the network and their effect is apparently overshadowed by an increasing number of small-size pores with decreasing radius. In the case of the normal pore-size distribution, again the mean value for the permeability decreased for increasing irregularity of the pore system, whereas the standard deviation increased with respect to the mean value for the permeability up to a certain pore-size distribution (i.e., a certain value for the mean pore radius). This again demonstrated the influence and the dominating effect of small-size pores on the macroscopic permeability. With continuing increase in irregularity of the pore system, discretization of the pore-size distribution and respective errors introduced into the analysis caused slight fluctuation of the numerical results.

Within future applications, the developed model shall be applied to other types of idealized pore-size distributions and will finally be employed to predict the macroscopic permeability of building materials based on pore-size information obtained from respective experiments.

REFERENCES

Carmeliet, J., Descamps, F., and Houvenaghel, G., A multi-scale network model for simulating moisture transfer properties of porous media, *Transport Porous Media*, vol. **35**, pp. 67–88, 1999.

Galle, C. and Daian, J. F., Gas permeability of unsaturated cement-based materials: Application of a multi-scale network model, *Mag. Concrete Res.*, vol. **52**(4), pp. 251–263, 2000.

Garboczi, E. J. and Bentz, D. P., Modelling of the microstructure and transport properties of concrete, *Construct. Build. Mater.*, vol. **10**(5), pp. 293–300, 1996.

Marchand, J. and Gerard, B., Microstructure-based models for predicting transport, penetration and permeability of concrete, H. W. Reinhardt, Ed., RILEM Report No. 16, London: E & FN Spon, pp. 41–81, 1997.

Mehta, P. K. and Manmohan, C., Pore size distribution and permeability of hardened cement paste, 7th International Congress on the Chemistry of Cement, Paris, vol. **3**, pp. 1–5, 1980.

Sandouki, H. and van Mier, J. G. M., Meso-level analysis of moisture flow in cement composites using a lattice-type approach, *Mater. Struct.*, vol. **30**, pp. 579–587, 1997.

Sutera, S. P. and Skalak, R., The history of Poiseuille's law, *Annu. Rev. Fluid Mech.*, vol. **25**, pp. 1–19, 1993.

Wikipedia, en.wikipedia.org/wiki/Hagen–Poiseuille_equation (Download: Sept. 2009).

Ye, G., Lura, P., and van Breugel, K., Modelling of water permeability in cementitious materials, *Mater. Struct.*, vol. **39**, pp. 877–885, 2006.

Zeiml, M., Concrete subjected to fire loading — from experimental investigation of spalling and mass-transport properties to structural safety assessment of tunnel linings under fire. PhD thesis, Vienna University of Technology, Vienna, 2008.

International Journal for Multiscale Computational Engineering 8(1), 113–129 (2010)

EFFECTS OF HIGH TEMPERATURE ON MESOSCALE PROPERTIES OF CONCRETE

Petr Kabele, Jaroslav Pekař, & Jiří Surovec*

Czech Technical University in Prague, Faculty of Civil Engineering, Thákurova 7, 166 29 Praha 6, Czech Republic

*Address all corespondence to P. Kabele E-mail: petr.kabele@fsv.cvut.cz

This paper presents a complete experimental methodology for identification of parameters that are necessary for mesoscale numerical modeling and analysis of damage and degradation of concrete at high temperatures. For this purpose, a series of specialized mesoscale experiments are devised and carried out. The experiments target mechanical and fracture properties as well as characteristics of heat transfer of the main mesoscopic phases of concrete, namely, cement mortar, limestone aggregate, and their interface. The tests are conduced on samples that were exposed both to room environment and high temperatures. Results are presented in terms of temperature-dependent material characteristics.

KEY WORDS: *elastic modulus, tensile strength, compressive strength, fracture energy, coefficient of thermal conductivity, specific heat, coefficient of thermal expansion, temperature dependence*

1. INTRODUCTION

Damage of concrete exposed to high temperatures, such as those arising from fire, is associated with complex physical and chemical phenomena. Considering the scale of concrete structures on one hand, and the composition of concrete on the other, it is convenient to study these phenomena on the mesoscale, while perceiving concrete as a two-phase composite consisting of cementitious mortar (matrix), coarse aggregate (inhomogeneities), and their interfaces. The most important mechanisms that cause degradation of concrete at elevated temperatures can be identified as follows:

1. Differential thermal expansion due to steep temperature gradients and different coefficients of thermal expansion of the constituent materials (namely, mortar and aggregate)

2. High internal pressures due to the release of capillary and chemically bound water, its evaporation, and movement through the porous structure (namely of mortar)

3. Thermo-chemo-mechanical changes of the constituent materials, such as dehydration of the hydrate calcium silicate (~180°C) or decomposition of the calcium hydroxide (~500°C) and of the hydrate calcium silicate (~ 700°C)

To be able to predict the macroscopic behavior of concrete exposed to fire and to possibly optimize its composition for better fire resistance, it would be desirable to understand the independent effects of the individual mechanisms. However, when concrete specimens of standard dimensions (on the order of 100 mm) are tested for the effects of high temperature on material behavior, e.g., strength, it is almost impossible to isolate the above-mentioned phenomena. This is obvious in the case of different thermal expansion coefficients of the constituents, or in the case of their different thermochemical degradation. But to also eliminate the effects of thermal gradients, concrete specimens would have to be heated at very slow rates. Similarly, to suppress the influence of pore vapor pressure and moisture transport, prolonged drying of samples prior to testing and again very slow heating would be necessary.

1091-028X/10/$35.00